Limiting shapes of confined lipid vesicles

B. Kavčič,*[a] A. Sakashita,[b,c] H. Noguchi,[c] and P. Ziherl[d,e]

Received Xth XXXXXXXXXX 20XX, Accepted Xth XXXXXXXXX 20XX
First published on the web Xth XXXXXXXXXX 200X
DOI: 10.1039/b000000x

We theoretically study the shapes of lipid vesicles confined to a spherical cavity, elaborating a framework based on the so-called limiting shapes constructed from geometrically simple structural elements such as double-membrane walls and edges. Partly inspired by numerical results, the proposed non-compartmentalized and compartmentalized limiting shapes are arranged in the bilayer-couple phase diagram which is then compared to its free-vesicle counterpart. We also compute the area-difference-elasticity phase diagram of the limiting shapes and we use it to interpret shape transitions experimentally observed in vesicles confined within another vesicle. The limiting-shape framework may be generalized to theoretically investigate the structure of certain cell organelles such as the mitochondrion.

1 Introduction

As the main building block of most forms of life, lipid membranes and vesicles remain one of the fundamental topics in biophysics. Even when studied at the mesoscopic level where their detailed molecular composition is subsumed by effective parameters such as the bending constant, the behavior of vesicles viewed as 2D surfaces is amazingly complex. In multicomponent vesicles, segregation of the components can lead to elaborate patterned spherical, budded, tubular, and starfish vesicles[1] and their thermal manipulation can be employed to drive vesicle self-replication.[2] The cornucopia of vesicular formations of non-trivial genus has only barely been explored,[3–5] and the same applies to vesicle-vesicle adhesion.[6] These problems are related to the structure of several cell organelles such as the Golgi apparatus and the nucleus, much like the understanding of the binding of a small colloidal particle at a membrane[7,8] is clearly important in endocytosis.

Another structural aspect typical of intracellular vesicular formations is confinement. For example, the inner membrane of the mitochondrion is enveloped by the outer membrane of a much smaller area, and it is plausible that the area mismatch is an important mechanism leading to the many folds characteristic of the inner membrane and known as cristae. The other two strongly folded and partitioned organelles, the endoplasmic reticulum and the Golgi apparatus, are not encompassed by a membrane but it is possible that the surrounding cytosol contributes towards an effective confinement by exerting pressure on them. In all three cases, folds are likely also stabilized by membrane self-adhesion, but a purely steric confinement still remains the most plausible non-specific mechanism responsible for folding.

In stark contrast with their relevance for the biological function of intracellular structures, the insight into the shapes of confined vesicles is fairly limited. The first systematic theoretical study of the problem dealt with a vesicle of vanishing spontaneous curvature within a spherical cavity, finding that it transforms from an axisymmetric stomatocyte to a non-axisymmetric stomatocyte and then to a non-axisymmetric double stomatocyte as the packing fraction is increased.[9] These results were then extended to ellipsoidal cavities and to vesicles with non-zero spontaneous curvature[10]; later the effect of the intrinsic vesicle shape was more comprehensively explored within the area-difference-elasticity (ADE) theory.[11] Also studied within the Helfrich theory of membrane elasticity were vesicles in spherical and cylindrical confinement adhering to the cavity[12] and the shapes of toroidal vesicles within a spherical cavity, which are either axisymmetric or non-axisymmetric and are characterized by double-sickle cross-section.[13] The simplest experimental system close to these models is a vesicle trapped within another vesicle. While they may be often accidentally seen in laboratory, controlling and systematically studying vesicles trapped in larger vesicles is very challenging, and only a few reports exist so far. In a recent observation of spontaneous deformation of such a vesicle, two sequences of shapes consistent with theoretical predictions were seen.[11]

Although the body of knowledge contained in the above numerical studies is hardly complete, a certain hierarchy is discernible in the reported shapes and shape transitions. The

[a] *Institute of Science and Technology Austria, Am Campus 1, A-3400 Klosterneuburg, Austria. E-mail: bor.kavcic@ist.ac.at.*
[b] *Department of Physics, Ochanomizu University, 2-1-1 Otsuka, Bunkyo, Tokyo 112-8610, Japan.*
[c] *Institute for Solid State Physics, University of Tokyo, Kashiwanoha 5-1-5, Kashiwa, Chiba 277-8581, Japan.*
[d] *Faculty of Mathematics and Physics, University of Ljubljana, Jadranska 19, SI-1000 Ljubljana, Slovenia.*
[e] *Jožef Stefan Institute, Jamova 39, SI-1000 Ljubljana, Slovenia.*

aim of this paper is to theoretically interpret this hierarchy in terms of the so-called limiting vesicle shapes.[14] The limiting shapes may be viewed as prototypes of a given class of shapes: For example, a free vesicle consisting of two spherical buds connected by a vanishingly narrow neck is the limiting shape of the pear class. As such, locations of limiting shapes in the phase diagram represent boundaries between the various classes each typically characterized by a different number of compartments, and this is why the analysis of limiting shapes is very helpful.

Inspired by the numerical results,[9–11] we construct the confined limiting shapes from simple geometric forms including primarily flat, cylindrical, and spherical surfaces as illustrated in Fig. 1. The shapes are described by one or two parameters which determine their respective locations in the phase diagram. In confined vesicles, this scheme appears to be increasingly more accurate as the packing fraction approaches unity and most of the cavity is occupied by the vesicle, offering a broad-stroke overview of the phase diagram. Here we elaborate the limiting-shape description of confined vesicles within the bilayer-couple and area-difference-elasticity theories and we show how it works in the case of spherical cavity; our results can be readily generalized to the spontaneous-curvature theory and to non-spherical cavities.

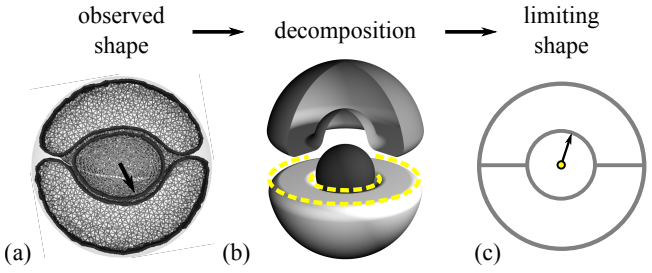

Fig. 1 Construction of the limiting-shape version of a three-compartment vesicle confined to a spherical cavity (a) obtained numerically using the approach reported in ref. 11. In the first step, we identify the most important morphological features of the vesicle, replacing it by an idealized shape (b) where the core compartment is spherical rather than oblate and the two shell compartments are identical, touching each other along a flat annulus between dashed yellow circles. Also visible are the internal and the external edges of the shell compartments. The corresponding limiting cap-cap-sphere shape (c) is parametrized by the radius of the core compartment indicated by the arrow, and the transverse curvature radii of the edges of the two shell compartments are assumed to be very small.

The disposition of the paper is as follows: In Section 2 we describe the main elements of the model, in Section 3 we use it to construct the limiting shapes of vesicles in spherical confinement, and in Section 4 we discuss their location in the bilayer-couple phase diagram. Section 5 is focused on the area-difference-elasticity phase diagram of confined vesicles, and in Section 6 the theoretical results are employed to interpret selected experimental and numerical data. Section 7 concludes the paper.

2 The model

Like many earlier studies,[15] we rely on the area-difference-elasticity (ADE) theory of vesicle shape.[14] In this theory, vesicle volume V and area A are fixed, and the shape of the vesicle is parametrized by the so-called reduced volume

$$v = \frac{V}{4\pi R_s^3/3} = \frac{6\sqrt{\pi}V}{A^{3/2}}, \tag{1}$$

where $R_s = \sqrt{A/4\pi}$ is the radius of the sphere of area A, and by the reduced monolayer area difference Δa defined by

$$\Delta a = \frac{1}{4\pi R_s}\oint H \mathrm{d}A. \tag{2}$$

Here $H = (C_1 + C_2)/2$ is the local mean curvature and the integral is over the whole vesicle. The equilibrium shape of the vesicle is determined by the local and the non-local bending energy. In the reduced form measured in units of the bending energy of a spherical vesicle equal to $8\pi k_c$, the local bending energy reads

$$w_b = \frac{W_b}{8\pi k_c} = \frac{1}{16\pi}\oint (2H)^2 \mathrm{d}A, \tag{3}$$

where k_c is the local bending constant. The non-local bending energy depends on the relative stretching of the two monolayers encoded by the difference between Δa and the preferred value of the reduced monolayer area difference Δa_0 determined by the difference in the numbers of the lipid molecules in the monolayers. The reduced non-local bending energy is given by

$$w_r = q(\Delta a - \Delta a_0)^2, \tag{4}$$

where $q = k_r/k_c$ is the ratio of the non-local and the local bending constants k_r and k_c, respectively.

In confined vesicles, the total bending energy

$$w_{\mathrm{ADE}} = w_b + w_r \tag{5}$$

is minimized at fixed v, Δa, and packing fraction given by the ratio of volumes of vesicle and cavity

$$\eta = \frac{V}{V_0} = 1 - \frac{\Delta V}{V_0}, \tag{6}$$

where V_0 is the volume of the cavity and $\Delta V = V_0 - V$ is the volume defect. Although it differs from that used in most earlier references in the field,[9,10,12,13] we choose the $(v, \Delta a, \eta)$ parametrization of confined vesicle shapes because it facilitates the comparison with free vesicles and because it relies on the packing fraction as a well-established and intuitive quantity.

2.1 Tight confinement approximation

It is natural to expect that the effect of confinement is most pronounced and thus probably most interesting if the packing fraction approaches 1. In this limit, the transverse curvature of the edges of vesicle compartments such as those shown in Fig. 1b is much larger than their lengthwise curvature; the former diverges at $\eta = 1$ and the latter scales with the radius of the cavity. As a result, the reduced volume v, the reduced monolayer area difference Δa, and the bending energy w_b can be calculated analytically or semi-analytically for many limiting shapes, which allows us to transparently study their relative stability and construct the phase diagram.

The tight confinement approximation is suitable for confined vesicles with η close to 1 and involves two simplifications. The main one pertains to the curvature of the edges, where we neglect the lengthwise curvature as if the edge were a part of a circular cylinder. In addition, we assume that the transverse curvature of all edges in the vesicle is the same; as implied by Fig. 1 it must depend on the packing fraction η and diverges for $\eta = 1$. These two assumptions allow for an approximate evaluation of Δa and w [eqns (2) and (5), respectively], which may be refined by including next-to-leading order terms if needed. In fact, as η approaches 1, this controlled approximation becomes exact because the bending energy is increasingly more dominated by the transverse curvature of edges which diverges at $\eta = 1$.

In the tight confinement approximation, the limiting shapes can be constructed from a small set of structural elements (Fig. 2):

- **External wall** is the part of the membrane that is in contact with the cavity; its area A_{ew} is typically just a little smaller than the area of the cavity, the difference being due to the external edges.

- **Internal walls** are the double-bilayer zones formed by invaginated parts of the membrane pushing against each other, and may be either flat or curved.

- **Edges** are the highly curved parts of the membrane where an internal wall meets the external wall (this is referred to as the external edge) or where either three or more internal walls meet (this is referred to as the internal edge); also possible are U-shaped internal edges terminating internal walls that do not cut across all of the vesicle.

- **Necks** are orifices connecting the different compartments of the vesicle. We assume that they are small and that their shape is catenoid-like with a vanishing mean curvature so that their contributions to Δa and w_{ADE} as well as to the membrane area and volume defect are negligible. In our theory, necks are implicit devices needed solely so that the compartments may exchange membrane area and volume.

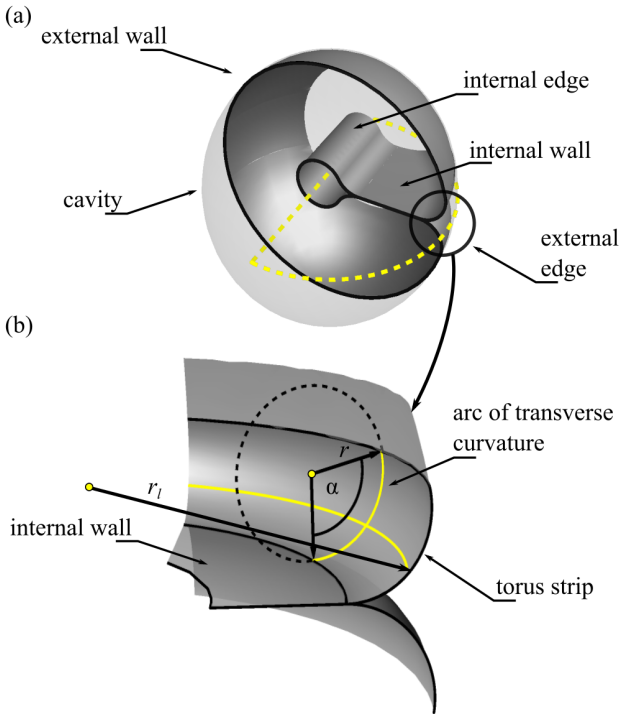

Fig. 2 Structural elements of limiting shapes (a) illustrated by a U-shaped vesicle consisting of the external wall, one flat internal wall reaching to the center of the cavity, one internal edge ending the internal wall, and one semicircular external edge. Dashed yellow lines indicate the contours of the edges for $\eta \to 1$. Panel b zooms in on the external edge, showing its contour (dashed yellow line of radius r_l) and transverse curvature (solid yellow arc of radius r and central angle α). In the tight confinement approximation, $r_l \gg r$.

Now we show how the reduced volume, the reduced monolayer area difference, and the reduced bending energy of vesicles contained within a cavity can be evaluated within the tight confinement approximation. One way or another, each of these quantities is related to an integral over membrane area which generally contains terms associated with all types of structural elements, but in v and Δa some of the terms are zero or vanishingly small. As elaborated below, v involves only the area of the walls, whereas Δa contains only terms corresponding to the external wall and to the edges.

2.2 Reduced volume

The reduced volume [eqn (1)] is a dimensionless quantity which depends on vesicle volume and area. For $\eta \to 1$, the volume defect ΔV is small compared to the cavity volume V_0 and the vesicle volume V can be approximated by V_0. As far

as the vesicle area is concerned, the membrane area in both external and internal edges is very small for $\eta \to 1$ since the transverse radius of the edges is much smaller than the cavity radius. Thus most of the vesicle area is contained in the internal and external walls. By definition, the reduced volume is given by $v = \eta V_0/(4\pi R_s^3/3)$, where $R_s = \sqrt{A/4\pi}$. For $V \approx V_0$ and a vesicle confined to a spherical cavity of radius $R_0 = \sqrt[3]{3V_0/4\pi}$, we have

$$v = \eta \left(\frac{R_0}{R_s}\right)^3. \tag{7}$$

Like in a free vesicle, the reduced volume of a confined vesicle with $\eta \to 1$ depends solely on its total area but not on its shape, number of compartments, etc.

2.3 Reduced monolayer area difference

The reduced monolayer area difference given by eqn (2) is an integral over all membrane area but the contribution of the internal walls is zero irrespective of their shape because the curvatures of the two bilayers in such a wall are equal and opposite. As a result, Δa contains only two terms — one associated with the external wall and the other associated with the edges. The first term reads

$$\Delta a_{\rm ew} = \frac{R_0}{R_s} = \left(\frac{v}{\eta}\right)^{1/3}, \tag{8}$$

where we used eqn (7). The edge term is somewhat more complicated. The mean curvature of an edge segment

$$H = \frac{1}{2}\left(\frac{1}{r} + \frac{1}{r_l}\right), \tag{9}$$

where r and r_l are the transverse and the lengthwise (principal) radii of curvature, respectively. Since r_l is typically of the order of R_0 and thus much larger than the transverse curvature of an edge, the lengthwise term in eqn (9) can be neglected and thus the mean curvature of an edge reads

$$H \approx \frac{1}{2r}. \tag{10}$$

In this study, we assume that the transverse radius of curvature r is the same in all edges. As shown in Sec. 2.4, the local bending energy is concentrated in the edges, and by choosing the same r we assume that this energy per unit area of the curved surfaces forming the edges is identical in all edges, which seems plausible.

The transverse edge radius can be estimated based on the volume defect and thus depends on the packing fraction. As illustrated by Fig. 3, the volume defect is contained solely in the edges, the contribution of an edge of length $L_{\rm ed}$ being given by $\Delta V_{\rm ed} = b_{\rm ed} r^2 L_{\rm ed}$ where $b_{\rm ed}$ is a dimensionless shape parameter characteristic of edge type. For a general three-way edge (Fig. 3b) it reads $b_3 = \sum_{i=1}^{3}(\tan\alpha_i/2 - \alpha_i/2)$ where $\sum_i \alpha_i = \pi$. The most common three-way edge is symmetrical where $\alpha_{1,2,3} = \pi/3$; in this case $b_{\rm se} = \sqrt{3} - \pi/2 \approx 0.16$. The external edge (Fig. 3a) can be viewed as a special case of a three-way edge with $\alpha_{1,2} = \pi/2$ and $\pi_3 = 0$ so that $b_{\rm ee} = 2(1 - \pi/4) \approx 0.49$; these values of α_i correspond to the packing fraction η very close to 1 where $r \to 0$ as shown below. In the U edge (Fig. 3c), $b_{\rm Ue} = \sqrt{3} + \pi/2 \approx 3.30$ which is considerably larger than $b_{\rm se}$ and $b_{\rm ee}$.

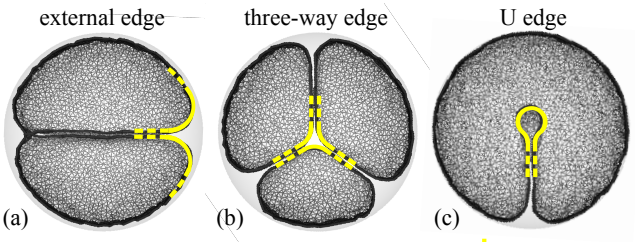

Fig. 3 Common edge types characteristic of limiting shapes: External edge (a), three-way edge (b), and U edge (c) shown in cutaway views of three numerically obtained vesicle shapes. The solid segment of the yellow lines represent the strongly curved membrane strips constituting an edge and the dashed yellow lines indicate the membranes of either external or internal walls that meet at an edge. The transverse curvature is positive in the external and the three-way edge and negative in the U edge. Note that the transverse-curvature radii are very similar in all edges in a given vesicle and that most of the volume defect is located at the edges. In panel a, the neck connecting the top and bottom compartment is visible in the left-hand side of the vesicle. The three shapes shown here were computed numerically as described in ref. 11.

The total volume defect is a weighted sum

$$\Delta V = r^2 \sum_i b_{\rm ed}^{(i)} L_{\rm ed}^{(i)} \tag{11}$$

over all edges. By recalling that $\Delta V = V_0(1-\eta)$ and $V_0 = 4\pi v R_s^3/3\eta$, we can now express the reduced transverse radius r measured in units of R_s as a function of η:

$$\frac{r}{R_s} = \sqrt{\frac{4\pi v(1-\eta)}{3\eta \sum_i \ell_{\rm ed}^{(i)} b_{\rm ed}^{(i)}}}. \tag{12}$$

Here $\ell_{\rm ed}^{(i)} = L_{\rm ed}^{(i)}/R_s$ is the reduced length of edge i. This result shows that in the tight confinement approximation where $\eta \to 1$, the ratio r/R_s vanishes which is quite intuitive.

Since $H \approx 1/2r$, the reduced monolayer area difference of a single strip in an edge (say one of the two seen in the external edge in Fig. 2b) can be approximated by $\Delta a_{\rm st} = {\rm sgn}(H) L^{{\rm sgn}(H)} \int_0^\alpha {\rm d}\varphi/8\pi R_s = {\rm sgn}(H)\alpha \ell^{{\rm sgn}(H)}/8\pi$,

where $\mathrm{sgn}(H)$ is the sign of the transverse curvature of the strip and the integral goes over the central angle subtended by the transverse cross-section of the strip α. As shown by this formula, Δa_{st} is proportional to reduced edge length and may be either positive or negative so that one must distinguish between the two cases; hence the superscript in the reduced edge length $\ell^{\mathrm{sgn}(H)}$. Any given edge consists of several strips and since their lengths are identical, it is best to combine their contributions to Δa in a single expression:

$$\Delta a_{\mathrm{ed}} = \mathrm{sgn}(\alpha_{\mathrm{ed}}) \frac{\alpha_{\mathrm{ed}}}{8\pi} \ell^{\mathrm{sgn}(\alpha_{\mathrm{ed}})}. \tag{13}$$

Here α_{ed} is a weighted sum the central angles of all membrane strips constituting the edge

$$\alpha_{\mathrm{ed}} = \sum_i \mathrm{sgn}(H_i)\alpha_i \tag{14}$$

and the edge curvature sign is defined by $\mathrm{sgn}(\alpha_{\mathrm{ed}})$.

Obviously, one needs to distinguish between edges of positive and negative transverse curvature because the corresponding Δa_{ed} differ in sign. There are two types of positive transverse-curvature edges: The external edge and the three-way edge of arbitrary symmetry*. In both of them, the signed sum of the central angles α_{ed} is π. As a result, the contributions of an external edge and a three-way edge of the same length to the total Δa of the vesicle are identical. Thus we can simply add their lengths L_i^+ and introduce the reduced total length of positive transverse-curvature edges:

$$\ell^+ = \frac{\sum_i L_i^+}{R_s} \tag{15}$$

so that eqn (13) reduces to $\ell^+/8$.

The only negative transverse-curvature edge considered here is the U edge (Fig. 3c) which is formed by an internal wall that does not cut entirely across the vesicle. Seen in Fig. 2a and Fig. 3c, this edge has a teardrop-shaped cross-section and consists of two identical positive transverse-curvature strips of central angles of $\pi/4$ attached to the internal wall and one negative transverse-curvature strip of central angle of $3\pi/2$ at the tip of the edge. Within our approximation where all transverse radii of curvature are the same, the central angles of the former are $\alpha_{1,2} = \pi/3$ and that of the latter is $\alpha_3 = -5\pi/3$ so that the combined $\alpha_{\mathrm{ed}} = -\pi$. Like in the positive transverse-curvature edges, we can add the lengths of all U edges and define the reduced total length of negative transverse-curvature edges by

$$\ell^- = \frac{\sum_i L_i^-}{R_s}. \tag{16}$$

The corresponding Δa_{ed} [eqn (13)] reads $-\ell^-/8$.

* Also possible are four-, five- ... way edges but in the limiting shapes considered here they do not appear.

Finally, the total reduced monolayer area difference of a vesicle is the sum of the two edge terms and the external-wall term [eqn (8)]:

$$\Delta a = \left(\frac{v}{\eta}\right)^{1/3} + \frac{\ell^+ - \ell^-}{8}. \tag{17}$$

2.4 Local bending energy

The local bending energy [eqn (3)] contains terms corresponding to all structural elements of the vesicle except necks and flat internal walls. The external-wall term is easiest of all: In reduced units, $w_b^{\mathrm{ew}} = 1$. Evaluation of the edge term is based on the same assumptions as the evaluation of Δa_{ed}, and the reduced local bending energy of a single edge reads

$$w_b^{\mathrm{ed}} = \frac{L_{\mathrm{ed}}}{16\pi} \sum_i \int_0^{|\alpha_i|} r^{-1} \mathrm{d}\varphi = \frac{\alpha_w L_{\mathrm{ed}}}{16\pi r}. \tag{18}$$

Here the sum is over all edge strips, α_is being the respective central angles, and $\alpha_w = \sum_i |\alpha_i|$. For both external and three-way edges $\alpha_w = \pi$ whereas for the U edge $\alpha_w = 7\pi/3$. By combining the terms corresponding to the three types of edges and by inserting eqn (12), we find that the total reduced bending energy of all edges in a vesicle is

$$w_b^{\mathrm{ed}} = \frac{1}{G}\sqrt{\frac{\eta \sum_i \ell_{\mathrm{ed}}^{(i)} b_{\mathrm{ed}}^{(i)}}{v(1-\eta)}} \left(\ell^+ + \frac{7}{3}\ell^-\right), \tag{19}$$

where $G = 32\sqrt{\pi/3} \approx 32.75$ is a numerical constant. As expected, w_b^{ed} diverges at packing fraction $\eta = 1$ where the radius of transverse curvature vanishes.

The reduced bending energy of the internal walls w_b^{walls} depends on their shape and size, and there exists no single general formula for all possible walls. In a few special cases, w_b^{walls} can be evaluated exactly, e.g., in a spherical internal wall characteristic of the double-stomatocyte (DS) shape discussed in Section 3 where $w_b^{\mathrm{walls}} = 2$ and in walls with zero mean curvature (say in a flat or a catenoidal wall) where $w_b^{\mathrm{walls}} = 0$. The total reduced local bending energy of a vesicle thus reads

$$w_b = 1 + \frac{1}{G}\sqrt{\frac{\eta \sum_i \ell_{\mathrm{ed}}^{(i)} b_{\mathrm{ed}}^{(i)}}{v(1-\eta)}} \left(\ell^+ + \frac{7}{3}\ell^-\right) + w_b^{\mathrm{walls}}. \tag{20}$$

Given that the non-local bending energy depends only on Δa, the above results can be used to evaluate the total ADE energy of the vesicle analytically or semi-analytically provided that the shapes of the internal walls are simple enough.

Together with the expressions for reduced volume and reduced monolayer area difference [eqns (7) and (17), respectively], eqn (20) constitutes a scheme that can be used to efficiently study the limiting shapes of confined vesicles. Before turning to these shapes themselves, we note that eqn (20)

alone shows that some of them must differ considerably in terms of the bending energy. In particular, given that the bending energy of the walls does not depend on the packing fraction, edgeless shapes such as the DS shape must be favored at $\eta \to 1$ compared to shapes with edges. Secondly, the bending energy of shapes that contain solely external edges [such as the cap-cap (CC) shape introduced in Section 3] is much smaller than that of shapes containing only U edges of the same length [such as the invaginated torocyte (IT_1) shape introduced in Section 3]. In the limit of $\eta \to 1$ where they are dominated by the edge terms, the ratio of energies of the two types of shapes reduces to $(3/7)\sqrt{b_{ee}/b_{Ue}} \approx 0.15$, which implies that the external-edge-only shapes should feature more prominently in the ADE phase diagram that the shapes containing only U edges. As shown in Section 5, this is indeed the case.

3 Limiting shapes

As already mentioned, limiting shapes proposed here are suitable idealizations of the experimentally and numerically observed shapes,[11] and some of them were included as their generalizations. The main classes of our limiting shapes grouped according to the number of compartments are shown in Fig. 4. The set is not exhaustive and there do exist additional classes such as the triple-invaginated torocyte analog of the double-invaginated torocyte shape in Fig. 4c and four-segment analogs of the three-segment shapes in Figs. 4h and i. Nonetheless we believe that the classes discussed here do cover the most interesting part of the phase diagram at Δa around 1.[14]

Most limiting shapes are parametrized by a single length — a distance, radius, or width — giving the location of an edge or, equivalently, the size of one or more walls. This length specifies both v and Δa as well as w_b at a given packing fraction η. Some shapes such as the offset U shape shown in Fig. 4a are described by two lengths or other geometric parameters as appropriate; technically speaking, they depart from the notion of limiting shapes known from free vesicles but are nonetheless included as natural and simple generalizations of certain single-parameter shapes. In Fig. 4, the parameters of the different classes are indicated by arrows†.

The limiting shapes can be grouped according to the number of compartments. If the reduced monolayer area difference is not large enough, the vesicle cannot be partitioned into two or more compartments (Fig. 4a-c). The simplest non-comparmentalized shape is the offset U shape (abbreviated by U′, Table 1) consisting of the external wall and an internal wall

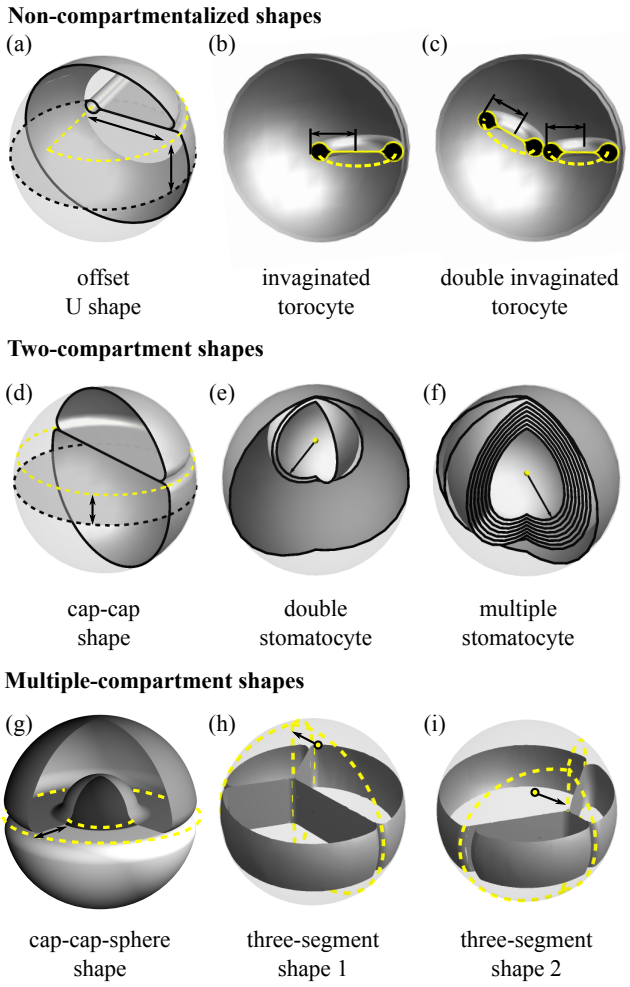

Fig. 4 Selected non-compartmentalized (top), two-compartment (middle), and three-compartment shapes (bottom) used in this study; the shapes themselves are described in the main text. Dashed yellow lines are the contours of the edges and arrows indicate the various lengths used to parametrize the shapes. The auxiliary black dashed line in panels a and d is the equator.

that does not protrude all the way through the vesicle lumen. The U′ shape has a straight U edge at the end of the internal wall and an arc-like external edge, and it is parametrized by the distance of the internal wall from the equator and by its width; the single-parameter symmetric version of the U′ shape where the internal wall is positioned right at the plane of the equator is referred to as the U shape. The two types of edges in the U′ shape may be regarded as a means of accommodating a given excess membrane area by creating a combination of negative and positive transverse-curvature edges. By completely contracting the positive transverse-curvature external edge and bending the negative transverse-curvature U edge, the U′ shape can be transformed into the invaginated-torocyte

† We refrain from introducing names or symbols for these parameters because their meaning is fairly obvious and because the details of the geometric analysis of the shapes, which are often tedious but mathematically straightforward,[16] are not included here.

shape	compartments	symmetry
invaginated torocyte (IT_1)	1	C_{2v}
double invaginated torocyte (IT_2)	1	C_{2v}
U	1	C_{2v}
offset U (U′)	1	C_{1v}
double stomatocyte (DS)	2	C_∞
multiple stomatocyte (DS_n)	2	C_∞
cap-cap (CC)	2	C_∞
valley cap-cap (CC_V)	2	C_{2v}
parabolic cap-cap (CC_P)	2	C_∞
saddle cap-cap (CC_S)	2	C_2
cap-cap-sphere (CCS)	3	$C_{\infty h}$
double cap-cap (CC_2)	3	$C_{\infty h}$
three-segment (TS_1, TS_2)	3	C_{2v}

Table 1 List of limiting shapes used with their respective abbreviations, number of compartments, and symmetry.

shape (IT_1; Fig. 4b) which has a smaller Δa than the U′ shape as suggested by eqn (17). Moreover, if the excess membrane area is partitioned into two rather than a single invaginated torocyte, the length of the U edge increases and thus Δa is decreased further; this is the double invaginated torocyte shape (IT_2; Fig. 4c). Both IT_1 and IT_2 shapes have a single parameter, namely the radius of the torocyte, and they may be expected at reduced volumes large enough so that the diameter of the invaginated torocyte fits into the cavity.

Alternatively, the limiting variant of the U′ shape where the wall stretches across all of the vesicle lumen is devoid of the U edge, the external edge forming a circle. In the obtained two-compartment cap-cap shape (CC; Fig. 4d) described solely by the distance of the internal wall from the equator, Δa is larger than in the U′ shape of the same v because the former does not contain a negative transverse-curvature U edge, and so ℓ^- in eqn (17) is 0. Numerical results[11] also suggest that the internal wall separating the two compartments in the CC shape may be curved rather than flat, and one thinks of three distinct wall bending modes each described by a suitable single-parameter quadratic function. In the saddle mode (CC_S shape), the normal displacement of the wall is given by $z = \alpha(x^2 - y^2)$, x and y being the in-plane coordinates, whereas in the valley mode (CC_V shape) $z = \alpha x^2$ and in the parabolic mode (CC_P shape) $z = \alpha(x^2 + y^2)$; the saddle mode is shown in the inset to Fig. 10 and the valley and parabolic modes can be seen in Fig. 1b in ref. 11. At a given v, these derivatives of the CC shape differ in the length of the external edge and thus in the value of Δa.

Another two-compartment shape obtained from the CC shape is the double-stomatocyte (DS) shape. The transformation between the two consists of a simultaneous contraction of the external edge to a point and the deformation of the flat internal wall of the CC shape to a spherical wall. This results in a shape with no edges (DS; Fig. 4e) and thus a low local bending energy of $w_b = 3$. In the DS shape, $\Delta a = (v/\eta)^{1/3}$ [eqn (17)], and the shape exists at all reduced volumes v larger than $3^{-3/2}$ where the diameter of the spherical internal wall is smaller than the diameter of the cavity. Below this v, multiple-stomatocyte shapes with $n > 1$ double-membrane spherical internal walls nested within each other are possible (DS_n; Fig. 4f), each again limited by the restriction that the internal wall fit in the cavity. In these shapes $\Delta a(v/\eta)^{1/3}$ and $w_b = 1 + 2n$. The simplest DS_n shape has a single multilamellar spherical wall and thus a single radius of invagination; this shape can be generalized to two-, three- etc. parameter shapes with different radii of double-stomatocyte invaginations, which need not be nested one within the other as long as their walls do not touch.

Multiple-compartment shapes are generally associated with a longer external or three-way edge, and thus a longer ℓ^+ and a larger Δa than the CC shape. The three-compartment double cap-cap shape (CC_2; shown in cross-section in the right-top corner of Fig. 5) has an additional cap-like compartment at the south pole compared to the CC shape; the heights of the caps, here assumed to be identical, are the only parameters of the CC_2 shape. The cap-cap-sphere shape (CCS; Fig. 4g) consists of two hemispherical shell-like compartments encompassing a spherical compartment of variable radius, whereas in the three-segment shapes the wedge-like compartments share a straight symmetric 120°–120°–120° three-way edge. Here we study two variants of such shapes, one with two large and one small segment and the other with one large and two small segments (TS_1 in Fig. 4h and TS_2 in Fig. 4i, respectively). Both shapes are parametrized by the distance of the three-way edge from the center.

All of the proposed limiting shapes are listed in Table 1 together with the abbreviations of their names, the number of compartments, and symmetry.

4 Bilayer-couple phase diagram

In the bilayer-couple (BC) model, the ratio of non-local and local bending constants q [eqn (4)] is infinite. As a result, Δa must be equal to Δa_0 and thus for the most part, vesicle shapes vary continuously from point to point in the $(\Delta a, v)$ phase diagram. The single-parameter limiting shapes represent the discontinuities in the phase diagram where the number of compartments and/or the symmetry of a given shape change, which is why they are so helpful.

Some aspects of the relative location of the different limiting shapes may be inferred from the way they are derived from each other in Section 3, but the global hierarchy of the shapes is best appreciated in the BC phase diagram (Fig. 5) plotted at $\eta = 1$ where the tight confinement approximation is exact and comparison with free vesicles is more straight-

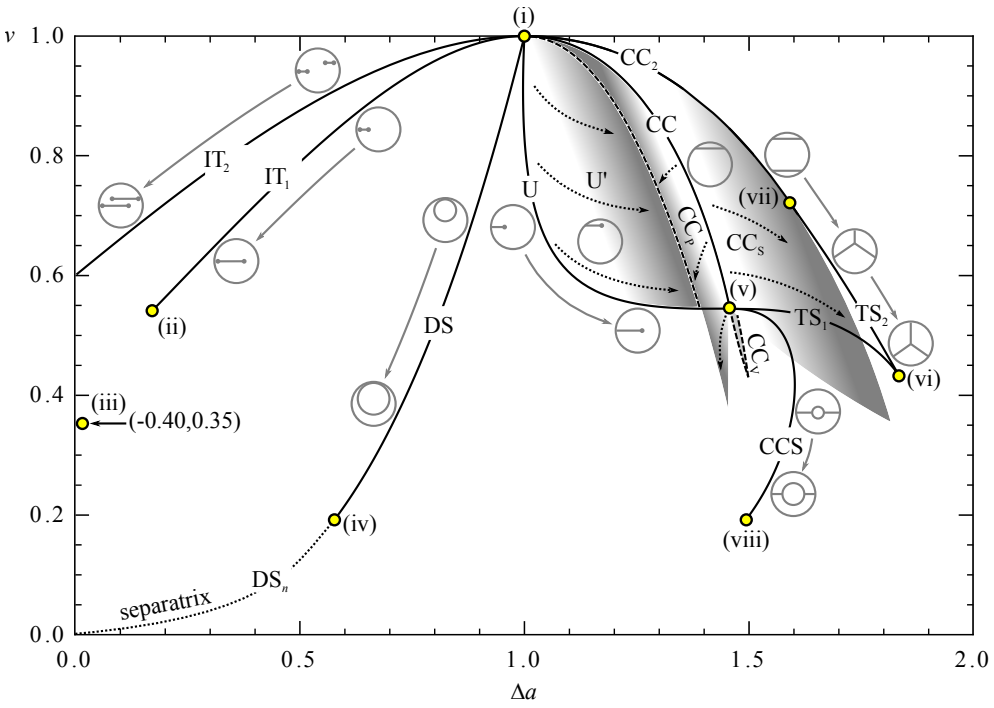

Fig. 5 $(\Delta a, v)$ phase diagram of vesicles confined to a spherical cavity at packing fraction $\eta = 1$. Solid lines represent the limiting shapes listed in Table 1, their endpoints (i)-(viii) highlighted by yellow circles; endpoint (iii) which terminates the IT_2 line is off the figure. Most single-parameter limiting shapes are illustrated by two representative cross-sections showing how they change as their respective parameters are increased as indicated by gray arrows. The dotted line is the $\Delta a = v^{1/3}$ separatrix. The shaded regions belong to the two-parameter shapes, where the shade of gray represents the increase of the secondary parameter. Even though the effects of wall modulation in the CC_V, CC_P, and CC_S shapes is calculated only approximately, the shades end where $\alpha = 1$. The inaccuracy of the approximation increases along the dashed arrows, which indicate how a given shape changes as the secondary parameter (the displacement of the internal wall in the U′ shape and the magnitude of wall modulation α in the CC_V, CC_P, and CC_S shapes) is increased from 0.

forward. In the phase diagram, the single-parameter limiting shapes are represented by lines connecting two endpoints of a higher symmetry; for example, endpoints (i) and (iv) of the DS line correspond to the sphere regarded as a DS with a vanishingly small invagination and a DS where the radius of the invagination is the same as the radius of the cavity, respectively. Each of the four two-parameter shapes (U′, CC_V, CC_P, and CC_S) occupies one of the shaded regions.

The topology of the phase diagram can be easily understood by resorting to eqn (17) which states that at a given v and $\eta = 1$, $\Delta a = v^{1/3}$ in the DS/DS_n shapes which have no edges. This line may be viewed as a separatrix because in the shapes where the total length of negative transverse-curvature edges exceeds the total length of positive transverse-curvature edges (i.e., $\ell^+ - \ell^- < 0$), $\Delta a < v^{1/3}$. As a result, these shapes are located left of the separatrix; conversely, shapes with $\ell^+ - \ell^- > 0$ and thus $\Delta a > v^{1/3}$ lie to the right of the separatrix. The separatrix connects the bottom-left corner of the diagram where $v = 0, \Delta a = 0$ with the top-center point $v = 1$, $\Delta a = 1$ representing the sphere.

Within our scheme, most shapes considered contain either only negative or only positive transverse-curvature edges and are thus clearly divided into two categories, the sole exceptions being the hybrid U′ shape and the edgeless DS and DS_n shapes. In the top part of the phase diagram at reduced volumes above endpoints (ii) and (v) of the IT_1 and CC lines at $v = (3/2)^{-3/2} \approx 0.54$, the phase sequence barely depends on v. A horizontal cut across Fig. 5 shows that the sequence of limiting shapes contains the IT_2 – IT_1 – DS – U – CC – CC_2 shapes; below endpoint (vii) at $v = (4/5)^{3/2} \approx 0.72$ where the two internal walls of the CC_2 shape approach each other so that the volume of the central compartment vanishes, the CC_2 shape is replaced by the TS_2 shape. We stress that the above sequence is open-ended: There do exist triple, quadruple... invaginated torocyte shapes to the left of the IT_2 line as well as three, four... compartment variants of the CC_2 and TS_2 shapes to the right of the CC_2/TS_2 line.

The shaded regions between the U and the CC_2/TS_2 shapes can be regarded as a next-order layer of analysis and are occupied by the two-parameter U′, CC_V, CC_P, and CC_S shapes.

At this point, our results are partial because we only discuss two-parameter derivatives of the U and the CC shape. Evidently, one can think of various curved-internal-wall variants of most if not all flat-internal-wall shapes such as the IT_1 and the CC_2 shape; alternatively, the walls of the CC_2 shape may be tilted relative to one another and the CCS shape may be generalized by displacing the flat internal wall between the shell-like compartments towards one of the poles as shown in Fig. 1 and more clearly in Fig. 1b of ref. 11. While these additional derivative shapes may be readily constructed, we expect that because of steric constraints their importance is somewhat more limited compared to U′, CC_V, CC_P, and CC_S shapes. For example, the magnitude of the saddle-shape modulation of the two flat internal walls in the CC_2 shape should not be too large so as to ensure that they do not intersect.

At reduced volumes below $v \approx 0.54$ corresponding to endpoints (ii) and (v) but above $v = 3^{-3/2} \approx 0.19$ corresponding to endpoints (iv) and (viii), the sequence of single-parameter shapes no longer includes the IT_1 and the CC limiting shapes. The IT_2 shape exists at v's no smaller than $v = 2^{-3/2} \approx 0.35$ whereas the two three-segment shapes TS_1 and TS_2 persist down to $v = (4/7)^{3/2} \approx 0.43$. As a result, the central part of the phase diagram contains solely the DS and the CCS shape flanked by either IT_2 or IT_3 shape (the latter not shown) on the small-Δa side and by either TS_1/TS_2 shapes or their four-compartment variants (again the latter not shown) on the large-Δa side depending on reduced volume. Also found at v's smaller than 0.54 are the CC_V, CC_P, and CC_S two-parameter derivatives of the CC shape.

Many shapes discussed above are closely related to their free-vesicle analogs, and it is instructive to examine the similarities and the differences between the limiting shapes of free and confined vesicles for $\eta \to 1$ in more detail. The correspondence is interesting by itself and it may also be helpful for the interpretation of any experimentally or numerically observed confined vesicles, which will invariably lie in between the two extremes. In Fig. 6, this comparison is carried out separately for the $\Delta a < 1$ and $\Delta a > 1$ shapes.

The IT and IT_2 shapes are directly based on free-vesicle shapes with one and two spherical invaginations, respectively. As shown in the inset in Fig. 6a, the single-invagination shape can be continuously transformed into the IT shape by decreasing the radius of the cavity to a point where the volume of the invagination vanishes and the invagination itself is reduced to a circular internal wall whose Δa is negative and larger in magnitude that that of the original spherical invagination. This can be done at constant vesicle volume and area, and thus in this process each point on the dashed line of single-invagination free vesicle shapes labeled by *S* moves to a smaller value of Δa as the packing fraction reaches 1. Of course, this is only possible at $v > 0.54$ where the IT shapes exist. In the same way,

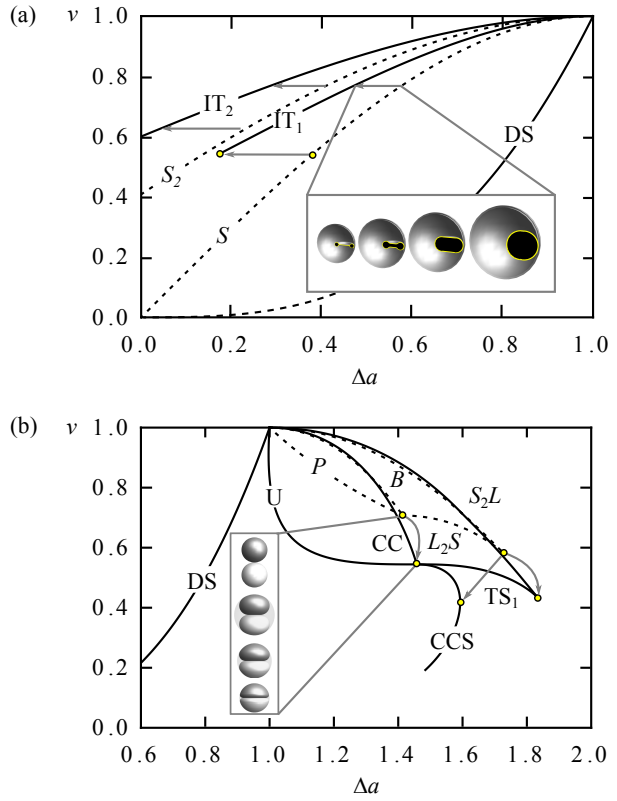

Fig. 6 Comparison of limiting shapes of confined (solid lines) and free vesicles (dashed lines; abbreviations in italics explained in the main text). Panel a shows the $\Delta a < 1$ part of the phase diagram where an invaginated limiting free-vesicle shape can be transformed into the corresponding invaginated-torocyte confined-vesicle shape at constant reduced volume as illustrated by the schematic sequence in the inset. The confined DS shape has no free-vesicle analog. In the free and confined $\Delta a > 1$ shapes shown in panel b, a one-to-one correspondence exists between the free-vesicle single-evagination *B* shape and the CC shape as well as between the lens-like double-dome *DD* shape and the U shape, whereas in other shapes the correspondence is more involved. The inset shows how a symmetric two-bud free shape is transformed into the symmetric CC confined shape, and that v is decreased in the process. Gray arrows connect the corresponding endpoints of the free and confined shapes.

double-invagination free vesicles lying along the S_2‡ dashed line are transformed into the IT_2 shape. — Note that the DS shape has no free-vesicle analog. One could, of course, construct a limiting shape with an evaginated and an invaginated bud of the same size but at $\Delta a = 1$ characteristic of this shape free vesicles assume a slightly stomatocytic shape instead.[14]

In a similar fashion, the evaginated limiting shapes of free vesicles can be related to their compartmentalized confined analogs. However, the $\Delta a > 1$ shapes cannot be confined at

‡ Abbreviations of the different free vesicle shapes are typeset in italics so that they may be more easily distinguished from the shapes of confined vesicles.

constant reduced volume. This is illustrated by the sequence of shapes in the inset in Fig. 6b starting with a free vesicle consisting of identical spherical buds as the extreme case of the single-evagination shape. Upon confinement at constant volume, the area of the buds must be increased or else their shape cannot be deformed, and thus the reduced volume of the vesicle is decreased. This is why the endpoint of the CC line which corresponds to a symmetric vesicle consisting of identical hemispherical compartments is located at a smaller v than the endpoint of the lines of single-evagination free vesicle shapes and pear shapes[§] (dashed lines B and P, respectively); also somewhat changed is the reduced monolayer area difference. Apart than this, the CC confined shapes are directly related to the single-evagination free shapes.

The analogies between free and confined three-compartment shapes are somewhat more complicated. The double-evagination free shape with two large and one small bud (L_2S) can be transformed either into the axisymmetric CCS shape or into the nonaxisymmetric TS_1 shape, which is also indicated by two arrows leading from the common endpoint of the free three-bud shapes L_2S and LS_2 to the endpoint of the TS_1 line and the rightmost apex of the CCS line where the volumes of the three compartments are identical. As far as the relative volumes of the compartments are concerned, the segment of the CCS line below this point corresponds to double-evagination free shapes with two small and one large bud (LS_2). In turn, the free LS_2 shape can also be transformed into the CC_2 and the TS_2 shape but the range of CC_2 shapes where the volumes of the caps are larger than the volume of the central part correspond to the free L_2S shapes. For clarity, only some rather than all of these relations are indicated in Fig. 6b.

Finally, we pause at the U shape which may be regarded as a confined version of the lens-like double-dome (*DD*) free vesicle shape consisting of two spherical caps.[14] On confinement, this shape would naturally transform into an incomplete CC shape with an opening in the internal wall and a U edge running around it. But it turns out that the energy of such a shape is always larger than that of the U shape at the same v and Δa and since there exists a smooth transformation between the two, we conclude that the U shape is derived from the *DD* shape.

5 Area-difference-elasticity phase diagram

The relative location of the limiting shapes in the BC phase diagram depends only on their geometric properties, and the diagram itself can be used to determine the sequence of shape classes obtained as either v or Δa are varied in an experiment or in direct numerical minimization of the vesicle free energy. For a more quantitative insight into the possible shape transition, we use the limiting shapes to construct the ADE phase diagram of confined vesicles. Naturally, the limiting shapes are generally not the lowest-bending-energy representatives of their respective classes *per se*. Still they do agree rather well with many of the numerically obtained shapes as seen by comparing Fig. 4 to the snapshots in Fig. 1b in ref. 11 (which may be due to the constraints imposed by severe confinement), and so we expect that their ADE phase diagram should nonetheless be quite relevant.

To this end, we minimize the combined ADE energy [eqn (5)] by choosing among the various single- and two-parameter shapes, each with a different w_b and a different Δa, at fixed v, Δa_0, and a large packing fraction η where the tight confinement approximation is valid. This is done numerically on a discrete mesh with steps of width 0.0014 and 0.009 along the v and Δa_0 axis, respectively. To facilitate comparison with the numerical results presented in ref. 11, the ratio of nonlocal to local bending constants q is set to π, which is close to typical values in lipid membranes.

Figure 7 shows the phase diagram at large packing fractions $\eta = 0.92$ and 0.96. For clarity, the CC shape and its two-parameter derivatives CC_V, CC_P, and CC_S shapes are shown as a single class of shapes, and so are the two versions of the three-segment shapes TS_1 and TS_2. The spikes/notches seen in the boundary of the CC class are an artifact introduced by the three distinct two-parameter shapes and should be smoothed out by hybrids combining morphological details of two or all of these shapes, which may well be observable numerically. All shape transitions shown are discontinuous.

Our Fig. 7 reproduces the overall topology as well as many quantitative features of the numerically obtained ADE phase diagram[11] although in the latter η is not constant but varies across the $(v,\Delta a)$ plane so that comparison is nontrivial. In particular, we find that at large enough v (i.e., above $v \approx 0.73$ and 0.82 in Figs. 7a and b, respectively) the transition between the invaginated non-compartmentalized to compartmentalized shapes takes place via the U′ shape rather than via the DS shape. Another robust feature of the ADE phase diagram seems to be the band-like domain occupied by the CC shape and its derivatives, which stretches across a broad range of reduced volumes at Δa_0 roughly between 1 and 2. The CCS shape is located at small v and large Δa_0 and the large-v, negative-Δa_0 part of the diagram contains increasingly more sophisticated invaginated shapes as Δa_0 is decreased, which is also consistent with the numerical results.[11] Finally, by plotting the ADE phase diagram at $\eta = 0.92$ and 0.96 we also show how the different classes of shapes advance into each other or retract as η is increased. Here the main effect is the expansion of the DS domain at the expense of the others, which nicely complements the numerical results covering the $\eta < 0.91$ range and reported in ref. 11. This is easy to under-

§ Pear shapes consist of two truncated spheres of identical radii.[14]

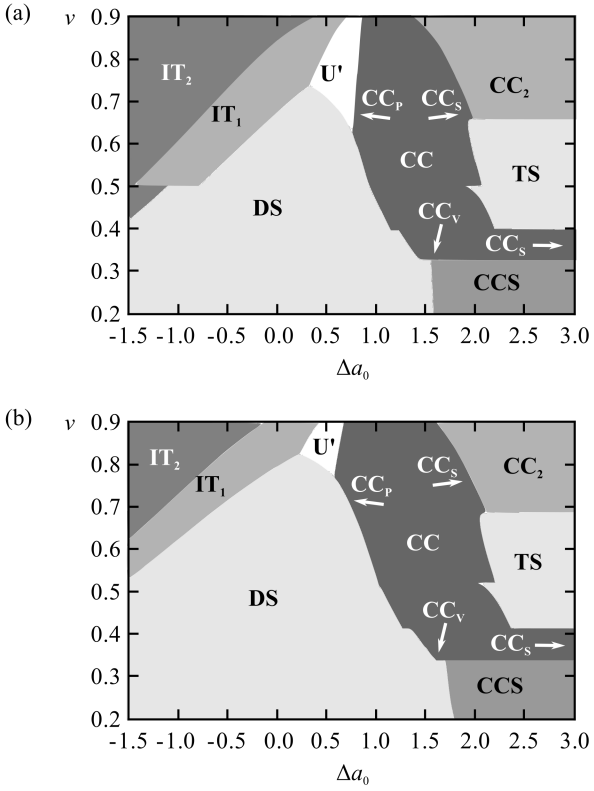

Fig. 7 ADE phase diagram of limiting shapes at two large packing fractions $\eta = 0.92$ (a) and $\eta = 0.96$ (b). All transitions are discontinuous; the CC_V, CC_P, and CC_S labels in the CC region indicate where the respective two-parameter derivatives of the CC shape is stable, the white arrows showing the direction of the increase of the secondary shape parameter.

stand as the local bending energy of DS shape is independent of the packing fraction whereas in all other shapes it diverges at $\eta = 1$ due to the ever larger bending energy stored in the edges.

6 Discussion

The transitions predicted by our theoretical phase diagram should well be observable experimentally, say in a vesicle confined within another vesicle and trapped in a microfluidic diffusion chamber.[17] Here the exchange of solvent between the fluid and the different compartments of the vesicle can be triggered by a sudden change in the osmolarity of the surrounding fluid. As a result, the packing fraction is changed too and this can drive shape transitions in a controlled fashion, allowing one to analyze the phase diagram systematically. So far such an experiment has not been performed yet; instead, shape transitions have been seen in confined vesicles undergoing spontaneous deformation attributed to the release of tight membrane folds created during vesicle formation.[11] In one case, an offset U shape deformed into an almost symmetric CC shape within a period of 7 s, which was attributed to an increase of Δa_0.

Here we present another spontaneous shape deformation of this type so as to provide further support of our theoretical considerations. We studied single-component DOPC (1,2-dioleoyl-*sn-glycero*-3-phosphocholine, Avanti Polar Lipids) vesicles prepared using the gentle hydration method[18,19] and dyed with TR-DHPE (Texas Red, 1,2-dihexadecanoyl-*sn-glycero*-3-phosphoethanol-amine, Molecular Probes). Observations were performed with a fast confocal microscope (Carl Zeiss, LSM 5Live) at room temperature (24-25°C). Figure 8 shows three snapshots of the transformation pathway from the DS shape to the IT_1 shape and then to an invaginated starfish.

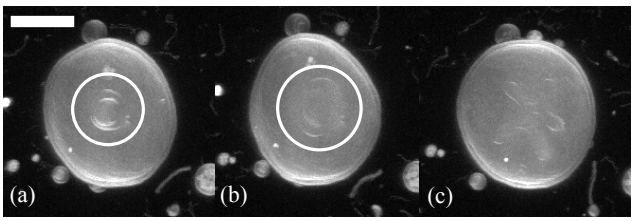

Fig. 8 Three snapshots of a spontaneous deformation of a DOPC vesicle confined within another almost spherical DOPC vesicle: The double-stomatocyte (DS) shape (a; $t = 0$ s), the invaginated torocyte (IT_1) shape (b; $t = 3$ s), and the invaginated starfish shape (c; $t = 14$ s). Bar indicates 10 μm; images were processed using ImageJ (FiJi) software to enhance contrast. Circles in panels a and b highlight the invaginated double stomatocyte and torocyte, respectively.

The two transitions can be quantitatively analyzed by assuming that the packing fraction and the reduced volume of the confined vesicle are constant during the process. These two quantities are easily estimated in the initial DS shape which, apart from the necks, can be approximated by three spherical surfaces. In this case, the packing fraction $\eta = 1 - (R_1/R_0)^3 + (R_2/R_0)^3$, where R_0 is the cavity radius whereas R_1 and R_2 are the radii of the primary and the secondary invagination, respectively. Based on the measured values of the three radii, we find that the packing fraction $\eta \approx 0.97$. In turn, the reduced volume of the whole vesicle is $v = \left[1 - (R_1/R_0)^3 + (R_2/R_0)^3\right]\left[1 + (R_1/R_0)^2 + (R_2/R_0)^2\right]^{-3/2}$ which gives $v \approx 0.79$. At the same time, during the shape transformation it is only the invaginated part of the membrane that changes its shape while maintaining its integrity as a single internal wall. This internal wall may be treated as a separate entity of a certain reduced volume given by $v_{\rm in} = v(1-\eta)/(\eta^{2/3} - v^{2/3})^{3/2}$;[11] in the shapes shown in Fig. 8, the estimated value of $v_{\rm in} \approx 0.53$. This is the first qualitative conclusion reached because free vesicles indeed

do form starfish shapes at small enough reduced volumes, $v_{\rm in}$ being roughly consistent with the onset of three-arm starfish shapes.[20,21]

Although not included in our range of limiting confined vesicle shapes, the invaginated starfish vesicle can be readily introduced as a generalization of the IT_1 shape. Recall that the main structural element of the IT_1 shape is a circular U edge, which spans the internal wall and carries a negative Δa as shown in Section 2. The volume defect contained in the U edge and the membrane area of the wall may be rearranged so as to form one or more discoidal torocyte-like protrusions, possibly arranged in a branched structure (Fig. 9). In the tight confinement approximation, such protrusions contribute a negative term to the total reduced monolayer area difference without affecting the vesicle area, the corresponding term being given by $\Delta a = -\ell^F/4$ where ℓ^F is the combined length of the protrusions. — We note in passing that these protrusions may be used as an additional structural element which decreases Δa of a given shape at fixed v, and that there must exist a considerable degeneracy because both Δa and w_b of such shapes should depend only on the total length of the protrusions but not on their number and relative lengths.[22]

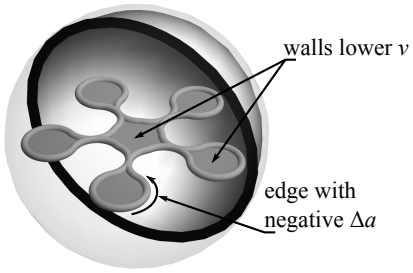

Fig. 9 Several invaginated torocytes arranged in a branched structure. In the tight confinement approximation, the edges of such a structure can accommodate a large negative monolayer area difference and carries a bending energy, both proportional to the length of the edge whereas the membrane area contained in the walls lower the reduced volume v.

Now we can roughly calculate the reduced monolayer area difference of the invaginated starfish by measuring the radius and the length of its arms, and the estimated Δa of the whole vesicle is ≈ -0.26. In a similar fashion, we estimated its local bending energy $w_b \approx 10.4$. The reduced monolayer area differences for the DS and the IT_1 shape are determined by the reduced volume and the packing fraction alone using the formulae in Section 2, and we then used these estimates as inputs in the ADE theory to determine the values of Δa_0 where the DS-IT_1 and the IT_1-invaginated starfish transitions take place. We find that the former is at $\Delta a_0 \approx -0.96$ and the latter is at $\Delta a_0 \approx -1.33$; here we assumed that $q = 2$ consistent with an earlier study of DOPC vesicles.[18] In this way, the limiting-shape framework can be employed to quantify the observed shape transformations in confined vesicles.

The limiting shapes can also be quantitatively compared to the numerically obtained results. As mentioned above, most of the known exact energy-minimizing shapes do agree with one of the limiting shapes in their large features,[11] but a detailed comparison is still in order. Here we focus on the two-compartment CC shape in a spherical cavity at a fixed $\Delta a_0 = 2$ and two large packing fractions of $\eta = 0.85$ and 0.9. Using the dynamically-triangulated membrane model,[23] we computed the vesicle shape for reduced volumes from 0.5 to 0.78 (at $\eta = 0.85$) and from 0.6 to 0.9 (at $\eta = 0.9$), measuring the asymmetry of the shapes in terms of the ratio of volume of the smaller compartment V_1 and the total vesicle volume V.

The overall behavior of V_1/V measured in the numerically obtained shapes is close to the theoretical prediction (solid line in Fig. 10) combining the CC shape at $v > 0.54$ and its CC_S derivative at $v < 0.54$, both at $\eta = 1$. The choice of the CC_S shape shown in the top-right inset to Fig. 10 was motivated by the numerically obtained shape in the bottom-left inset. In view of the approximations made in the limiting shapes, the agreement found is rather good given that the packing fractions of the numerical and the limiting shapes are not exactly the same. In the simulations, there exists a finite spacing both between the external vesicle wall and the cavity and between the membranes in an internal wall. Short-range excluded volume interactions between the vertices of the mesh as well as between the vertices and the cavity must be introduced to avoid the penetration of the membranes and the thermal undu-

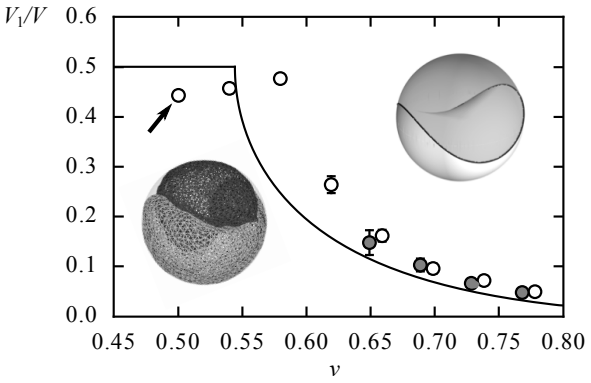

Fig. 10 Relative volume of the smaller compartment in the two-compartment shape vs. reduced volume at fixed $\Delta a_0 = 2$. Points show numerical results for $\eta = 0.85$ and 0.9 (open and filled circles, respectively); errorbars are not shown where smaller than symbol size. Solid line is the theoretical relative volume of $\eta = 1$ CC and CC_S shape at $v > 0.54$ and $v < 0.54$, respectively. The insets show the numerically obtained and theoretical CC_S shape at $v = 0.5$ (arrow).

lations yield the membrane repulsion since the thermal fluctuations are included in the simulations ($k_c = 20k_BT$). These finite distances prevent exceedingly large edge curvatures so that the vesicle shape containing slightly longer edges is preferred to the limiting shape at $\eta = 1$. However, such effects are rather small as shown in Fig. 10. A similar comparison can be made for several other shapes.

7 Conclusions

The relevance of the limiting-shape framework for confined vesicles presented here is twofold. On one hand, it provides a global overview of the bilayer-couple phase diagram, showing which shape sequences may be observed as the geometric parameters of the vesicles are varied. At the same time, the limiting-shape approach complements numerical studies of the problem in the regime of large packing fractions where the search for exact energy-minimizing vesicle shapes is increasingly more difficult due to severe confinement; in addition, it does so at a fraction of the computational effort.

The spectrum of limiting shapes proposed above is centered at the crossover from non-compartmentalized to compartmentalized shapes and may readily be extended both by including additional structural elements and by the various additional two-parameter shapes. It may also be adapted to vesicles confined to non-spherical confining geometries as well as to floppy cavities. Furthermore, the limiting-shape framework can be generalized by including adhesion either between the vesicle and the cavity or between the different parts of the vesicle itself. Yet another possible extension would be to apply it to self-adhering vesicles which should assume a spherical external form so as to minimize the non-contact membrane area if the adhesion strength were large enough — much like adhering vesicle doublets.[6] In this respect, self-adhering vesicles should be quite similar to vesicles confined to a spherical cavity.

When viewed from a distance, the problem of confined vesicles bears some similarity to several instances of shape formation in biological systems, say to the folding of epithelial tissues attached to an elastic substrate[24] or to the mechanics of gut formation[25] and even to the packing of DNA in viral capsids.[26] As such, the results presented here do not only lay the ground for a better theoretical insight into the form and structure of membrane-based cell organelles such as the mitochondrion and the Golgi apparatus but also contribute to the understanding of the different mechanisms involved in morphogenesis in general.

Conflict of interest

There are no conflicts of interest to declare.

Acknowledgments

We thank M. Imai for permission to use micrograph in Fig. 8 taken in his laboratory, and we acknowledge the financial support from the Slovenian Research Agency (research core funding No. P1-0055) and from the female leadership program at Ochanomizu University.

References

1 T. Baumgart, S. T. Hess and W. W. Webb, *Nature*, 2003, **425**, 821–824.
2 T. Jimbo, Y. Sakuma, N. Urakami, P. Ziherl and M. Imai, *Biophys. J.*, 2016, **110**, 1551–1562.
3 X. Michalet and D. Bensimon, *Science*, 1995, **269**, 666–668.
4 H. Noguchi, *EPL*, 2015, **112**, 58004.
5 H. Noguchi, *Biophys. J.*, 2016, **111**, 824–831.
6 P. Ziherl and S. Svetina, *Proc. Natl. Acad. Sci. USA*, 2007, **104**, 761–765.
7 M. Deserno, *Phys. Rev. E: Stat., Nonlinear, Soft Matter Phys.*, 2004, **69**, 031903.
8 S. Dasgupta, T. Auth and G. Gompper, *Nano Lett.*, 2014, **14**, 687–693.
9 O. Kahraman, N. Stoop and M. M. Müller, *EPL*, 2012, **97**, 68008.
10 O. Kahraman, N. Stoop and M. M. Müller, *New J. Phys.*, 2012, **14**, 095021.
11 A. Sakashita, M. Imai and H. Noguchi, *Phys. Rev. E: Stat., Nonlinear, Soft Matter Phys.*, 2014, **89**, 040701(R).
12 J. E. Rim, P. K. Purohit and W. S. Klug, *Biomech. Model. Mechanobiol.*, 2014, **13**, 1277–1288.
13 L. Bouzar, F. Menas and M. M. Müller, *Phys. Rev. E: Stat., Nonlinear, Soft Matter Phys.*, 2015, **92**, 032721.
14 S. Svetina and B. Žekš, *Eur. Biophys. J.*, 1998, **46**, 13–137.
15 U. Seifert, *Adv. Phys.*, 1998, **17**, 101–111.
16 B. Kavčič, *MSc thesis*, Faculty of Mathematics and Physics, University of Ljubljana, 2014.
17 S. Vrhovec, M. Mally, B. Kavčič and J. Derganc, *Lab Chip*, 2011, **11**, 4200–4206.
18 A. Sakashita, N. Urakami, P. Ziherl and M. Imai, *Soft Matter*, 2012, **8**, 8569–8581.
19 J. P. Reeves and R. M. Dowben, *J. Cell. Physiol.*, 1969, **73**, 49–60.
20 W. Wintz, H.-G. Döbereiner and U. Seifert, *EPL*, 1996, **33**, 403–408.
21 P. Ziherl and S. Svetina, *EPL*, 2005, **70**, 690–696.
22 X. Michalet, *Phys. Rev. E: Stat., Nonlinear, Soft Matter Phys.*, 2007, **76**, 021914.
23 H. Noguchi and G. Gompper, *Phys. Rev. E: Stat., Nonlinear, Soft Matter Phys.*, 2005, **72**, 011901.
24 E. Hannezo, J. Prost and J.-F. Joanny, *Phys. Rev. Lett.*, 2011, **107**, 078104.
25 T. Savin, N. A. Kurpios, A. E. Shyer, P. Florescu, H. Liang, L. Mahadevan and C. J. Tabin, *Nature*, 2011, **476**, 57–62.
26 A. Leforestier, A. Šiber, F. Livolant and R. Podgornik, *Biophys. J.*, 2011, **100**, 2209–2216.